Chemical Science

ROYAL SOCIETY OF CHEMISTRY

EDGE ARTICLE

View Article Online
View Journal | View Issue

Check for updates

Cite this: *Chem. Sci.*, 2023, **14**, 8905

All publication charges for this article have been paid for by the Royal Society of Chemistry

Received 23rd May 2023
Accepted 16th July 2023

DOI: 10.1039/d3sc02595k

rsc.li/chemical-science

Chalcogen-doped, (*seco*)-hexabenzocoronene-based nanographenes: synthesis, properties, and chalcogen extrusion conversion†

Ranran Li,[a] Bin Ma,[a] Shengtao Li,[a] Chongdao Lu [a] and Peng An *[ab]

A series of chalcogen-doped nanographenes (NGs) and their oxides are described. Their molecular design is conceptually based on the insertion of different chalcogens into the hexa-*peri*-hexabenzocoronene (HBC) backbone. All the NGs adopt nonplanar conformations, which would show better solubility compared to planar HBC. Except for the oxygen-doped, saddle-shaped NG, the insertion of large chalcogens like sulfur and selenium leads to a *seco*-HBC-based, helical geometry. All the three-dimensional structures are unambiguously confirmed by single-crystal X-ray diffractometry. Their photophysical properties including UV-vis absorption, fluorescence, chiroptical, charge distribution, and orbital gaps are investigated experimentally or theoretically. The properties of each structure are significantly affected by the doped chalcogen and its related oxidative state. Notably, upon heating or adding an acid, the selenium-doped NG or its oxide undergoes a selenium extrusion reaction to afford *seco*-HBC or HBC quantitatively, which can be treated as precursors of hydrocarbon HBCs.

Introduction

Polycyclic aromatic hydrocarbons (PAHs) have fascinated chemists for a long time due to their wide utility in materials science,[1] optoelectronic devices,[2] biological probes,[3] and supramolecular chemistry.[4] To exploit three-dimensional aesthetic structures and modulate optoelectronic or photophysical properties, an increasing number of contorted polycyclic aromatic hydrocarbons (PAHs) or nanographenes (NGs) have been developed in the past decades.[5] Such nonplanar PAHs or NGs have been constructed with a diversity of shapes, including bowls,[6] saddles,[7] helixes,[8] belts,[9] rings,[10] and hybrid conformations[11] by "bottom-up" strategies. Compared to their planar counterparts, nonplanar PAHs or NGs have shown intriguing properties including high solubility, different aggregation patterns, tunable optoelectronic properties, and specific supramolecular interactions.[3a,12] Strategically, the introduction of main-group elements into hydrocarbon PAHs is another powerful method to not only modulate their three-dimensional structures but tune their intrinsic properties including chemical reactivity, electronic energy gap, and photophysical behavior.[13]

As a planar NG unit, hexa-*peri*-hexabenzocoronene (HBC), a D_{6h} − symmetric planar π scaffold (Fig. 1a), and its derivative have been intensively studied.[14] Owing to the nature of its planar structure, HBC generally exhibits low solubility and a high aggregation tendency in solvents, which commonly hampers its application, particularly in solution-based device fabrication.[3a,15] Thus, numerous efforts have been made to engineer the structure of HBC. For example, by incorporation of a non-hexagonal ring like a seven-,[7a] eight-,[16] or nine-membered[17] ring into the HBC skeleton, saddle-, or helical-,

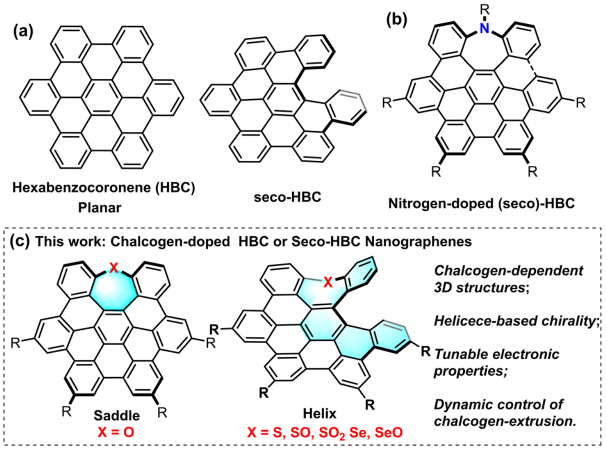

Fig. 1 (a) Structures of planar HBC and partially cyclized *seco*-HBC. (b) Structures of nitrogen-doped, (*seco*)-HBC-based NGs. (c) Insertion of chalcogens to design heteroatom-doped HBC or *seco*-HBCs.

---

[a] *School of Chemical Science and Technology, Yunnan University, Kunming 650091, P. R. China. E-mail: anp@ynu.edu.cn*

[b] *Key Laboratory of Medicinal Chemistry for Natural Resource, Ministry of Education, Yunnan University, Kunming 650091, P. R. China*

† Electronic supplementary information (ESI) available. CCDC 2238626–2238632. For ESI and crystallographic data in CIF or other electronic format see DOI: **https://doi.org/10.1039/d3sc02595k**

seco-HBC-based (Fig. 1a) structures were revealed, and these novel nonplanar structures exhibit distinct photophysical properties and aromaticity compared to the parent HBC. Recently, by insertion of nitrogen into the HBC backbone in the *fjord* region, our group reported nitrogen-doped HBC- or *seco*-HBC-based NGs[7b,18] (Fig. 1b), and the optical properties can be mediated by introducing versatile substituents at the peripheral nitrogen. In this context, we focused our attention on the insertion of chalcogens into the HBC backbone. We envisioned that varied chalcogens in the new backbone of NGs would significantly affect the properties of the entire π-system in the following aspects: (1) specific atomic radii of doped chalcogens may lead to diverse three-dimensional structures; (2) distinct electronegativities and multiple oxidation states of chalcogens would be beneficial to sophisticatedly tune the electronic properties; (3) by means of the unique chalcogen-extrusion reaction,[19] a specific reactivity toward atom-extrusion conversion would offer dynamic control of ring-reconstruction.

Thus, a series of chalcogen-doped NG analogs were designed and the influences of the doped chalcogens or oxidized chalcogens on the overall synthesis, structural geometry, electronic properties, and chalcogen extrusion reaction of the π-systems are demonstrated (Fig. 1c). Single-crystal X-ray analysis unequivocally reveals the saddle- and saddle–helix-shaped conformations of these novel chalcogen-doped NGs. The photophysical properties as well as the chiroptical properties of the helical, sulfur- and selenium-doped NGs were investigated. Meanwhile, thermal- or acid-induced chalcogen extrusion reactions for these NGs were studied, and the heteroatom-dependent chalcogen-extrusion processes were observed. Particularly, the selenium-doped NGs exhibit controllable, fast, and quantitative selenium extrusion conversion to form HBC under acidic conditions at room temperature. For the first time, the saddle–helix precursors of HBC, with over 100-fold higher solubility than HBC, were identified. The details of these results will be elucidated in this article.

Results and discussion

Synthesis of chalcogen-doped nanographenes

To obtain a series of chalcogen-doped NGs, we used a universal synthetic route to synthesize NGs with different alkyl side chains for single crystal cultivation (Scheme 1). In brief, the Diels–Alder reaction of dibenzo[*b*,*f*]oxepine (DBO) **1** with tetrabromothiophene-*S*,*S*-dioxide **2** in toluene followed by oxidative aromatization in the presence of 2,3-dichloro-5,6-dicyano-1,4-benzoquinone (DDQ) afforded tetrabrominated aromatics **3** in 75% yield. Subsequently, fourfold Suzuki–Miyaura cross-coupling reactions of compound **3** with (4-ethylphenyl) boronic acid in the presence of 15 mol% $PdCl_2(CH_3CN)_2$, 30 mol% SPhos and excess K_3PO_4 then furnished the hexaphenylbenzene **4** in 81% yield. The treatment of compound **4** with DDQ (10.0 equiv.) in the presence of triflic acid (13.0 equiv.) in DCM in a water-ice bath resulted in the fully fused oxa-NG $\mathbf{5_O}$ within 5 minutes in 65% yield with the formation of five new C–C bonds. For sulfur- or selenium-doped analogs, thiepine **8** and selenepine **9** were prepared in a two-step reaction with overall 58% and 24% yields respectively: the copper-catalyzed oxidative coupling of (2-formalphenyl) boronic acid with the sulfur or selenium followed by intramolecular McMurry olefin formation. Then Diels–Alder reactions of thiepine **8** and selenepine **9** with compound **2** followed by oxidative aromatization with DDQ furnished compounds **10** and **11** in 90% and 56% yields respectively. Notably, a higher temperature (140 °C in xylene) and longer reaction time are needed for selenepine **9** compared to that for oxepine **1** and thiepine **8** in the Diels–Alder reaction (synthetic details in the ESI†). Then arylations for compounds **10** and **11** were performed using Suzuki–Miyaura cross-coupling conditions in the presence of

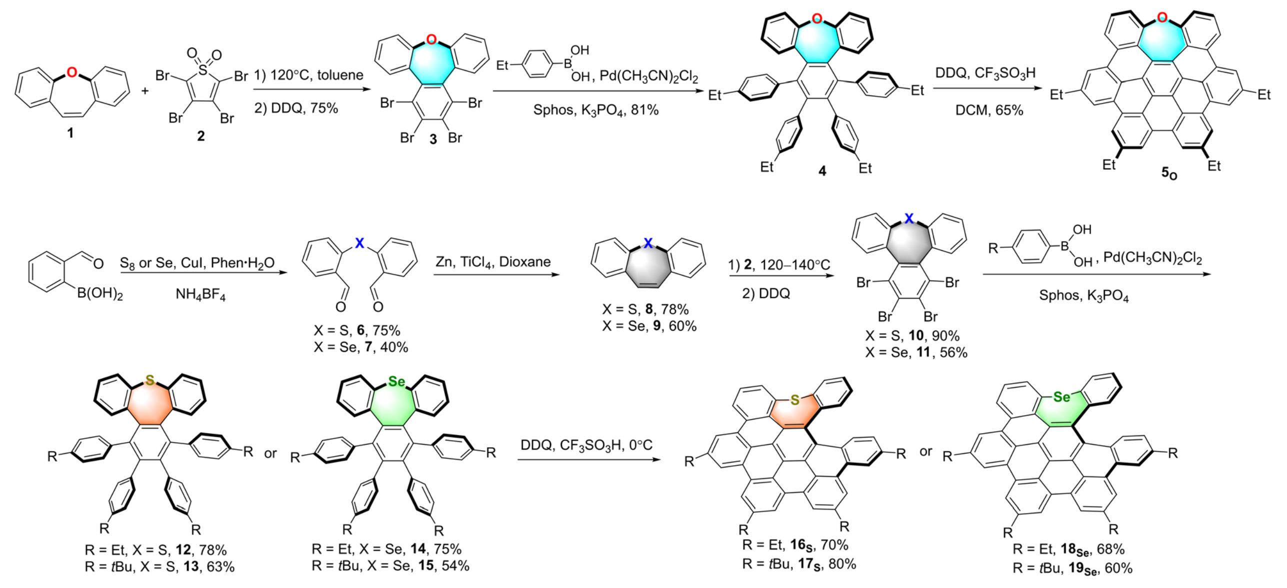

Scheme 1 Synthesis of oxygen-doped NG 5_O, sulfur-doped NGs 16_S, and 17_S, and selenium-doped NGs 18_{Se} and 19_{Se}.

15 mol% $PdCl_2(CH_3CN)_2$, 30 mol% SPhos, excess boronic acid, and K_3PO_4, affording hexaphenylbenzene **12–15** in 54–78% yields. When compounds **12–15** were subjected to Scholl reactions under the conditions of DDQ/CF_3SO_3H in DCM at 0 °C, the *seco*-HBC-based structures **16_S**, **17_S**, **18_{Se}**, and **19_{Se}** were obtained with the formation of four continuous C–C bonds. Instead of the fully cyclized saddle of oxygen-embedded NG, helical structures were formed for sulfur- and selenium-doped NGs presumably due to the large strain caused by atom size increasing. In any attempts of increasing the temperature, adding more equivalent reagents, or using other oxidative cyclization conditions, no fully fivefold cyclization product was observed (Scheme S6†). Meanwhile, the synthesis of tellurium-doped NGs was also investigated (Scheme S4†). In order to construct a tellurium-doped analog, we synthesized dibenzo[*b*,*f*]tellurepine **21** from dibromide **20** after failed attempts by using the same synthetic procedure as compounds **6** and **7** from boronic acid. Through two-fold lithium-halide exchange with *n*-butyl lithium followed by tellurium insertion, compound **20** was successfully transformed to dibenzo[*b*,*f*]tellurepine **21** in 58% yield. The mono-tellurium-doped aromatics **21** was unambiguously confirmed by X-ray crystallography analysis.[20] Subsequently, we subjected compound **21** to similar Diels–Alder reaction conditions by reacting with tetrabromide **2**. Consequently, no tellurium-insertion product **22** was detected by gradually raising the heating temperature. Instead, we observed phenanthrene formed as the dominant product through tellurium extrusion of compound **21** upon heating to 140 °C, and some amount of tetrabromo **23** was observed when the heating temperature raised up to 180 °C. These results indicated that telluride **21** is prone to undergo a tellurium extrusion reaction prior to the Diels–Alder reaction, and compound **23** was most likely formed by [4 + 2] cycloaddition of phenanthrene and compound **2**. Structure **23** was also confirmed by X-ray crystallography analysis.[20] Hence, the tellurium extrusion process suggested a higher possibility of heteroatom-extrusion by doping a larger-size chalcogen.

With the sulfur- and selenium-doped NGs in hand, their oxidative analogs were prepared (Scheme 2). The selective oxidation of sulfur-NGs **16_S** and **17_S** and selenium-NGs **18_{Se}** and **19_{Se}** was performed by treating them with oxone at 0 °C for 2 hours to afford the corresponding mono-oxides **24_{SO}** and **25_{SO}**, and **26_{SeO}** and **27_{SeO}** in nearly quantitative conversion. Meanwhile, the *S*,*S*-dioxide **28_{SO2}** was obtained by oxidation of compound **25_{SO}** at room temperature in the presence of an excess amount of *meta*-chloroperoxybenzoic acid (*m*-CPBA), while **27_{SeO}** cannot be oxidized under these conditions. Due to the highly distorted skeletons, all the chalcogen-doped NGs as well as the corresponding oxides show good solubility in organic solvents; therefore, they could be unequivocally confirmed by means of ^1H- and ^{13}C NMR spectroscopy (Fig. S29–S50†) and high-resolution mass spectrometry (see the ESI†). Meanwhile, the *seco*-HBC-type molecules including **16_S**, **18_{Se}**, and **24_{SO}** were further characterized by 2D ^1H–^1H ROESY and COSY (Fig. S1–S3†).

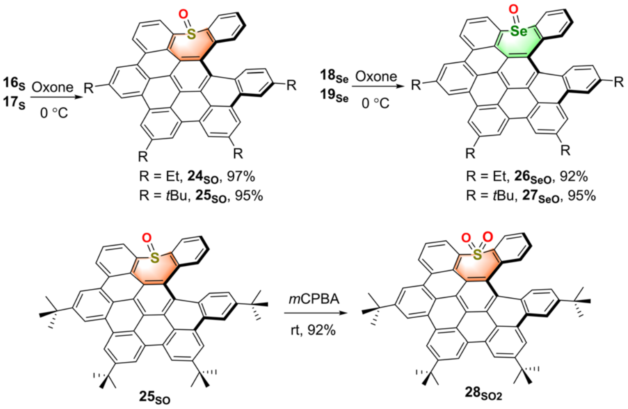

Scheme 2 Synthesis of oxidative derivatives of S-, Se-doped NGs.

Structural analysis of NGs

We next try to grow single crystals for all the NGs with different alkyl chains, and as a result, single crystals of **5_O**, **17_S**, **18_{Se}**, and **24_{SO}** suitable for X-ray diffraction analysis were obtained by slowly evaporating their solutions at room temperature (Tables S1 and S2†).[20] As shown in Fig. 2a–d, all the molecular backbones are distorted due to the incorporation of a heteroatom-doped, seven-membered ring. All the seven-membered rings exhibit different degrees of antiaromaticity suggested by nucleus-independent chemical shift (NICS)[21] by DFT calculations at the B3LYP/6-311+G(d,p) level of theory (Fig. S27†). Positive NICS (0) values between 2.79 and 6.49 were observed for all chalcogen-doped, seven-membered rings. The localized orbital locator (LOL)-π electron distribution calculation indicated that the electrons were localized on the seven hexagonal rings with strong π-conjugation (Fig. S27†). In detail, the X-ray crystallographic analysis of **5_O** reveals a saddle-shaped, negatively curved structure in which the oxygen atom protrudes from the π surface. Such a distorted conformation resembles that of a previously reported N–Me doped analog.[7b] The depths of the saddle, defined as the perpendicular distance from the centre of ring A to the line across C14 and C3 is 0.91 A (Fig. 2e), slightly shallower than the N–Me doped analogue. Meanwhile, the structures of **17_S**, **18_{Se}**, and **24_{SO}** exhibited saddle–helix geometry with a protruding chalcogen out of the π surface (Fig. 2b–d). The end-to-end dihedral angle of [5]helicene in NG **17_S** defined as the angle formed by the two benzene rings located at its terminal edges is 71.4°, and the torsion angle (C8–C14–C12–C38) is 34.9° (Fig. 2b). Meanwhile the dihedral angle and torsion angle in NG **18_{Se}** are 73.0° and 32.2° (C5–C4–C3–C2) respectively (Fig. 2c). Longer Se1–C1 (1.917 Å) and Se1–C35 (1.920 Å) bonds in **18_{Se}** were observed compared to C–S bonds (1.766 and 1.778 Å) in **17_S** due to the larger atomic radii of selenium. Both helicenes **17_S** and **18_{Se}** exhibited a larger end-to-end dihedral angle and torsion angle than the nitrogen-doped analogs (64.4° and 31.1° respectively)[18b] due to the increased atom size of sulfur and selenium. As helicenes, the crystallography of both **17_S** and **18_{Se}**, shown in Fig. 2f as a representative example, displays P/M enantiomers in single crystal structures (Fig. S5 and S6†). The *S*-oxide **24_{SO}** was also unequivocally

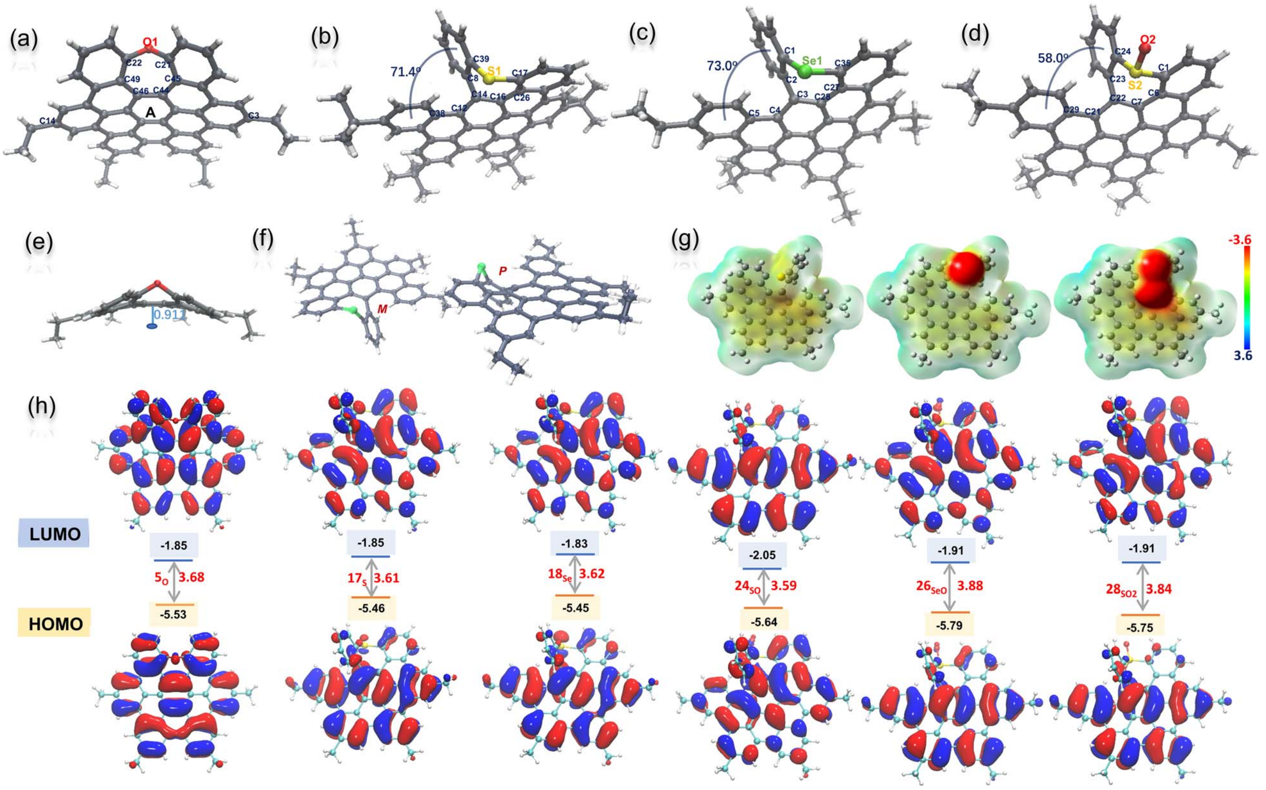

Fig. 2 X-ray crystallographic structures of $\mathbf{5_{O}}$ (a), $\mathbf{17_{S}}$ (b), $\mathbf{18_{Se}}$ (c), and $\mathbf{24_{SO}}$ (d) with 50% probability of thermal ellipsoids. Side view of the saddle-shaped NG $\mathbf{5_{O}}$ with the saddle-depth marked (e) and a pair of enantiomers shown in the single crystal $\mathbf{18_{Se}}$ (f). Electrostatic potential (ESP) maps and the energy colour bar (a.u.) of S-, SO-, and SO_2-doped NGs (g), in which the alkyl chains were replaced by methyl groups. TD-DFT calculation of HOMO and LUMO orbitals with energies (eV) of $\mathbf{5_{O}}$, $\mathbf{17_{S}}$, $\mathbf{18_{Se}}$, $\mathbf{24_{SO}}$, $\mathbf{26_{SeO}}$, and $\mathbf{28_{SO2}}$ at the PBE0/6-311G(d,p) level of theory (h). The alkyl chains were replaced by methyl groups.

confirmed by its X-ray structure (Fig. 2d). The formation of the SO bond decreased the end-to-end dihedral angle (58° in $\mathbf{24_{SO}}$) and torsion angle (29.8°, C23–C22–C21–C29). Due to the electronegativity of sulfoxide, the intermolecular hydrogen bond interaction between sulfoxide and dichloromethane was observed in the crystal packing besides the π–π stacking (Fig. S7†). The electron-static potential (ESP) map of $\mathbf{17_{S}}$, $\mathbf{24_{SO}}$, and $\mathbf{28_{SO2}}$ obtained through DFT calculations at the CAM-B3LYP/6-31+(d,p) level of theory (Fig. 2g) clearly showed the influence of different sulfur-oxidation states on the charge of the NG molecules. As expected, the electrons were distributed almost evenly on the surface of sulfur-doped NG $\mathbf{17_{S}}$, and aggregated at the oxygen once the sulfur was oxidized in $\mathbf{24_{SO}}$, and $\mathbf{28_{SO2}}$. The HOMO and LUMO orbitals[22] of *seco*-HBC-based NGs $\mathbf{17_{S}}$, $\mathbf{19_{Se}}$, $\mathbf{24_{SO}}$, $\mathbf{26_{SeO}}$, and $\mathbf{28_{SO2}}$ calculated at the PBE0/6-311G(d,p) level do not differ a lot from each other: each HOMO is found to be delocalized on the entire molecule, while the LUMOs are delocalized on the coplanar benzenoid rings (Fig. 2h).

Photophysical and electrochemical properties

The optical properties of chalcogen-doped NGs were investigated by UV-vis absorption and fluorescence spectroscopy. The UV-vis spectra of $\mathbf{5_{O}}$, $\mathbf{17_{S}}$, $\mathbf{19_{Se}}$, $\mathbf{25_{SO}}$, and $\mathbf{27_{SeO}}$ in DCM show that the absorption maxima are nearly identical (351–353 nm) together with multiple shoulder peaks, while sulfone $\mathbf{28_{SO2}}$ exhibits a red-shifted absorption band with the maximum peak at 360 nm (Fig. 3a). The weak absorption peaks of $\mathbf{5_{O}}$, $\mathbf{24_{SO}}$, and $\mathbf{26_{SeO}}$ with ethyl substituents at approximately 450 nm were observed rather than the *tert*-butyl substituted analogs probably due to the formation of an exciplex by intermolecular π–π interaction (Fig. S8†). To obtain insights into the origin of the absorptions, we conducted time-dependent density-functional theory (TD-DFT) (Fig. S28, Tables S10–S15†). The DFT calculations indicated that the lower-energy bands at around 430 and 400 nm are mainly contributed by the HOMO–LUMO transition. The high-energy bands at approximately 375 and 350 nm can be assigned to either HOMO–LUMO+1 or HOMO−1–LUMO and HOMO−1–LUMO+1 respectively, which exhibit larger oscillator strength. The fluorescence maximum of these NGs is similarly located at around 475 nm with shoulder emission peaks for $\mathbf{5_{O}}$, and a bathochromic-shifted peak at 490 nm for $\mathbf{28_{SO2}}$ was observed (Fig. 3b). These compounds exhibit a large Stokes shift of 120 nm (over 7200 cm^{-1}). Meanwhile, these chalcogen-doped NGs exhibit fluorescence intensity that depends on the doped heteroatoms and their oxidative state. With a similar helical conformation, $\mathbf{17_{S}}$ doped with sulfur exhibited 10-fold higher fluorescence intensity and nearly 20-fold higher fluorescence quantum yield (Table S3†) than the selenium-doped analog

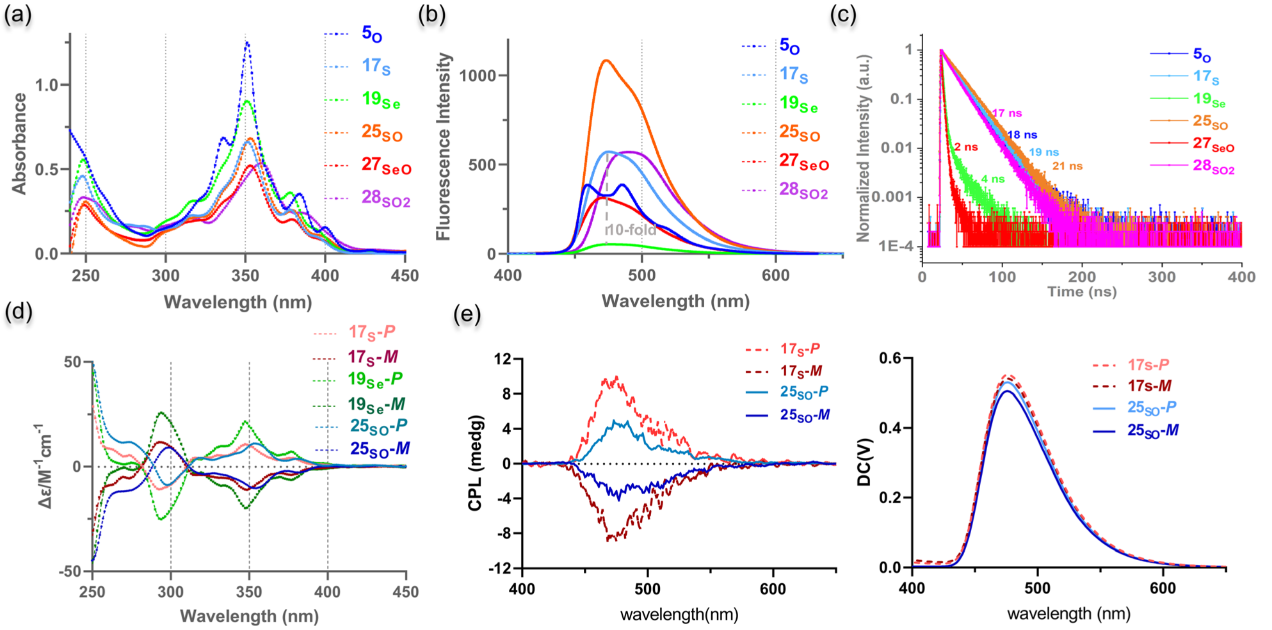

Fig. 3 Photophysical and chiroptical properties of chalcogen-doped NGs. (a) UV-vis absorption spectra, (b) fluorescence emission spectra, and (c) fluorescence decay profiles of 5_O, 17_S, 19_{Se}, 25_{SO}, 27_{SeO}, and 28_{SO2}. The spectra were collected in DCM solution with 5 μM concentration and $\lambda_{exc.} = 350$ nm for fluorescence excitation. (d) CD spectra of enantiomeric 17_S-P and 17_S-M, enantiomeric 19_{Se}-P and 19_{Se}-M, and enantiomeric 25_{SO}-P and 25_{SO}-M in hexane. (e) CPL and direct current (DC) spectra of 17_S-P/17_S-M and 25_{SO}-P/25_{SO}-M in dichloromethane ($\lambda_{exc.} = 350$ nm, the measurement was carried out in air).

19_{Se}. The fluorescence efficiency of NGs can be significantly enhanced by changing the doping heteroatoms S or Se to *S*-oxide or Se-oxide (**17_S** *vs.* **25_{SO}**; **19_{Se}** *vs.* **26_{SeO}**, Fig. 3b, Table S3†). As a result, the *S*-oxide **25_{SO}** was highly fluorescent with the highest fluorescence quantum yield of 0.30, which is significantly higher than that of the corresponding HBC **30_{HBC}** and *seco*-HBC **$29_{seco\text{-}HBC}$** (Table S3†). Notably, the difference in the magnitude of the fluorescence decay was observed by doping different heteroatoms. As shown in Fig. 3c, the oxygen- and sulfur-doped candidates **5_O**, **17_S**, **25_{SO}**, and **28_{SO2}** exhibit very close decay rates with fluorescence lifetimes over 17 ns, whereas, for selenium-doped compounds **19_{Se}** and **27_{SeO}**, the fluorescence lifetimes are less than 4 ns. Electrochemical properties were investigated by cyclic voltammetry in CH_2Cl_2 in the presence of Bu_4NPF_6 as a supporting electrolyte (Fig. S11†).

Notably, the redox properties can be modulated by controlling the oxidative states of the doped chalcogens. The oxidized structures **25_{SO}**, **27_{SeO}**, and **28_{SO2}** show more oxidation waves than their reduced analogs **17_S** and **19_{Se}**.

Chiroptical properties and determination of the racemization barrier

Helicene-based NGs have triggered much interest in the past decades due to their intrinsic chirality.[23] We attempt to resolve the two sets of enantiomers for both **17_S** and **19_{Se}** and study their chiroptical properties. The enantiomers of **17_S** and **19_{Se}** were successfully separated by chiral high-performance liquid chromatography (HPLC) at 25–30 °C with ethanol as the mobile phase (Fig. S12 and S13†). The electronic circular dichroism (ECD) spectra of the enantiomers of **17_S** and **19_{Se}** in hexane demonstrated a perfect mirror image relationship with multiple opposite Cotton effects in the UV/vis region from 200 to 450 nm (Fig. 3d). Due to the homologous chiral structures, similar profiles of enantiomers from **17_S** and **19_{Se}** were displayed. Each enantiomer of **17_S** or **19_{Se}** was confirmed by comparing each ECD spectrum with the calculated spectrum (Fig. S26†). Since sulfoxide **25_{SO}** shows high emission efficiency, we prepared the optically pure enantiomers **25_{SO}**-P/**25_{SO}**-M by oxidation of enantiomers **17_S**-P and **17_S**-M (Fig. S14†), and the ECD spectra of **25_{SO}**-P/**25_{SO}**-M indicated a perfect enantiomer relationship (Fig. 3d). Next, we carried out circularly polarized luminescence (CPL) measurements for each enantiomer. The CPL spectra of **17_S**-P/**17_S**-M and **25_{SO}**-P/**25_{SO}**-M exhibited a mirror-imaging relationship in dichloromethane under ambient conditions (Fig. 3e), which suggested that **17_S** and **25_{SO}** show CPL activity.

The luminescence dissymmetry ratio (g_{lum}), evaluating the degree of CPL, was determined to be 1.1×10^{-3} and 5.6×10^{-4} for **17_S** and **25_{SO}** respectively at 480 nm (Fig. S15†). Due to the low fluorescence quantum yield ($\Phi_F < 0.01$), the CPL of **19_{Se}**-P and **19_{Se}**-M was feeble to be detected. Meanwhile, due to the high extinction coefficient and Φ_F, the enantiomers of **17_S** and **25_{SO}** exhibit B_{CPL} up to 13 M^{-1} cm^{-1} and 12 M^{-1} cm^{-1} respectively. The successful resolution of two enantiomers of **17_S** or **19_{Se}** indicated relatively high enantiomerization barriers for both helicenes.

To experientially determine the isomerization barrier ($\Delta G^{\ddagger}$), thermal racemization of optically pure **17_S**-P was performed followed by chiral HPLC analysis (Fig. S16†). HPLC traces of the samples after heating at 100 °C exhibited a clean transformation from the **17_S**-P to the **17_S**-M isomer. The half-life ($\tau_{1/2}$)

for loss of enantiomeric excess was determined to be 5.5 hours at 100 °C. It gives a racemization barrier $\Delta G^{\ddagger}$ (373 K) of 29.6 kcal mol^{-1} using the Eyring equation, which demonstrated a relatively stable helicene enantiomer and comparable with reported [5]helicene containing NGs.[24] In addition, thermal racemization of optically pure $\mathbf{19_{Se}}$-P was performed similarly. However, $\mathbf{19_{Se}}$-P stayed stable after heating at 100 °C for hours, which suggested a higher isomerization barrier of $\mathbf{19_{Se}}$ than that of $\mathbf{17_{S}}$. Interestingly, the selenium-extrusion reaction was observed together with enantiomerization when the heating temperature was raised to 130 °C (Fig. S17†). Nevertheless, excluding other chemical reactivity, the racemization barrier $\Delta G^{\ddagger}$ of $\mathbf{19_{Se}}$ was evaluated to be 31.2 kcal mol^{-1} at 403 K.

Chalcogen-extrusion processes

After getting a hint from the observation of the selenium-extrusion process during the synthesis, we then investigated the chalcogen-extrusion reactions of these heteroatom-doped NGs. Several organosulfur compounds are susceptible to undergoing photo- or thermal-induced sulfur extrusion reactions.[25] Initially, we examined whether the extrusion reactions could be triggered by UV light. Each compound was treated in DCM solution under an atmosphere of N_2, followed by photo-irradiation with 254 or 365 nm UV light. Unfortunately, no distinct change was observed for all the NGs upon irradiation for a short period of time (<10 min) and compounds gradually degraded over a long time. Alternatively, we performed the thermal chalcogen extrusion for compounds $\mathbf{5_{O}}$, $\mathbf{17_{S}}$, $\mathbf{19_{Se}}$, $\mathbf{25_{SO}}$, $\mathbf{27_{SeO}}$, and $\mathbf{28_{SO2}}$ (Fig. 4a). The experiments were conducted by heating milligrams of solid of each sample in an oven for a specific time, and monitoring the changes in the absorption spectra after re-dissolving the preheated sample in DCM. To our delight, for selenium-doped candidates, $\mathbf{19_{Se}}$ and $\mathbf{27_{SeO}}$, identical de-selenium products were detected by observing the same absorption profiles formed after heating at 200 °C for only 5 min. These new species were confirmed as selenium-extrusion product $\mathbf{29}_{\boldsymbol{seco}\textbf{-HBC}}$ in comparison with the UV-absorption of standard product $\mathbf{29}_{\boldsymbol{seco}\textbf{-HBC}}$ (Fig. 4be). The HPLC analyses of the brown samples formed upon heating (Fig. 4b, inset) indicated a quantitative formation of $\mathbf{29}_{\boldsymbol{seco}\textbf{-HBC}}$ (Fig. S20 and S21†). In contrast, sulfur $\mathbf{17_{S}}$ and sulfone $\mathbf{28_{SO2}}$ as well as the oxygen-doped saddle $\mathbf{5_{O}}$ showed no change in the absorption spectra upon heating up to 250 °C for 2 hours, which suggests relatively thermally stable structures (Fig. 4c, f, and S18†). Meanwhile, sulfoxide $\mathbf{25_{SO}}$ exhibited an inert sulfur extrusion process by heating over 250 °C compared to selenium-doped analogs (Fig. 4d and S19†). These results suggested the accessibility and rate of chalcogen extrusion reaction are highly dependent on the sort and oxidative state of the embedded chalcogens.

The HBC reveals wide application in materials science but is detrimental to the fabrication of material devices due to aggregation-caused low solubility. Apparently, having a soluble precursor of HBC would significantly facilitate the material fabrication of HBC. We envisioned whether HBC structures could be obtained by spontaneous oxidative cyclodehydrogenation of the chalcogen-extrusion products. By screening commonly used acids like acetic acid, HCl, and trifluoroacetic acid, it was found that selenium oxide $\mathbf{27_{SeO}}$ could slowly convert to $\mathbf{30_{HBC}}$ in a trifluoroacetic acid/DCM (1/2, v/v) solution (Fig. 5a) and the formation of target product $\mathbf{30_{HBC}}$ was unequivocally confirmed by X-ray crystallography (Fig. 5b, Scheme S5†).[20] As monitored by UV-vis absorption (Fig. 5c), through selenium extrusion and spontaneous oxidation in air, the characteristic peak of $\mathbf{27_{SeO}}$ at 353 nm gradually shifted to

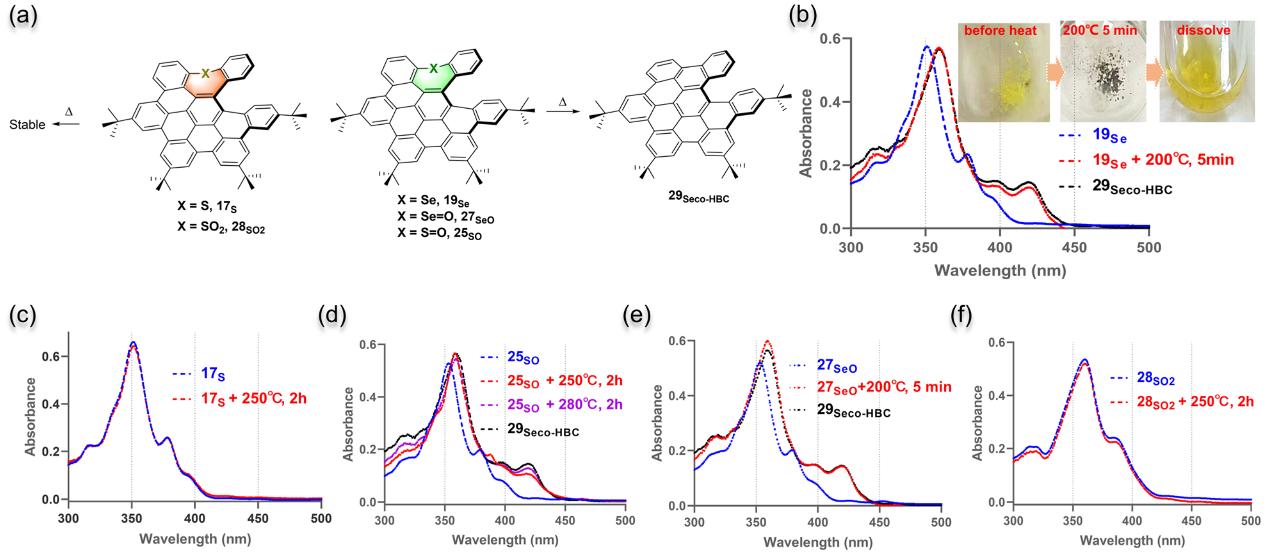

Fig. 4 (a) Chalcogen extrusion reactions of S-, Se-doped NGs. UV-vis absorption spectra of $\mathbf{19_{Se}}$ (b), $\mathbf{17_{S}}$ (c), $\mathbf{25_{SO}}$ (d), $\mathbf{27_{SeO}}$ (e), and $\mathbf{28_{SO2}}$ (f) before and after heating. The spectra were collected by dissolving the solid (before and after heating) in DCM and the heating time of each compound was shown in the corresponding spectrum. For comparison, the UV-vis spectra of the chalcogen-extrusion product $\mathbf{29}_{\boldsymbol{seco}\textbf{-HBC}}$ were shown together with $\mathbf{19_{Se}}$ (b), $\mathbf{25_{SO}}$ (d), and $\mathbf{27_{SeO}}$ (e). The inset in (b) shows the photographic images of the $\mathbf{19_{Se}}$ solid before and after heating, and the dissolved brown heated solid in DCM.

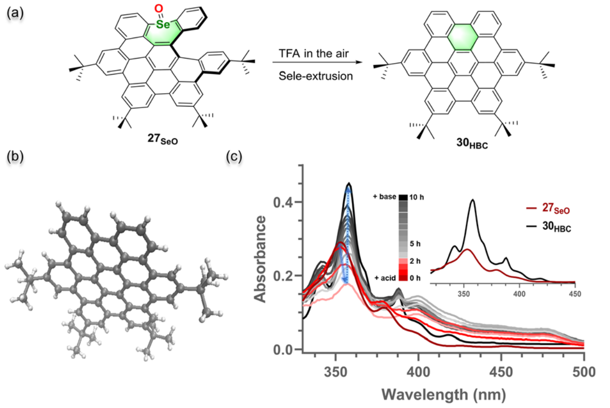

Fig. 5 (a) Acid-catalyzed HBC formation from HBC precursor selenium-doped NG 27_{SeO}. (b) X-ray crystallographic structure of 30_{HBC} with 50% probability of thermal ellipsoids. (c) Changes in the UV-vis absorption spectra of 27_{SeO} upon dissolving it in trifluoroacetic acid/DCM (1/2, v/v) with 3.3 μM concentration under ambient conditions.

358 nm over 20 hours in the trifluoroacetic acid/DCM (1/2, v/v) solution, and the absorption spectrum after a 20 hour reaction was almost identical to that of $\mathbf{30_{HBC}}$, whereas the other NGs were stable under these conditions (Fig. S23†). Together with the HPLC analyses (Fig. S22†), a nearly quantitative conversion was obtained for $\mathbf{27_{SeO}}$. Moreover, this transformation could be accelerated by the addition of stronger acid methanesulfonic acid instead of trifluoroacetic acid (Fig. S24†). To evaluate the difference in soluble properties between HBC and this precursor, we measured the solubility of $\mathbf{27_{SeO}}$ and $\mathbf{30_{HBC}}$ in dichloromethane and ethanol (Fig. S25†). The precursor $\mathbf{27_{SeO}}$ exhibits more than 100-fold higher solubility in either dichloromethane or polar solvent ethanol.

Conclusions

We have developed a new class of chalcogen-doped NGs, in which a chalcogen is conceptually embedded into the HBC or *seco*-HBC backbone in the *fjord* region. As a eesult of the size of chalcogens, two types of structures were obtained toward the final step of the oxidative ring closure reaction: the oxygen-doped saddle and the sulfur- or selenium-doped helix. The saddle and helical three-dimensional structures of the chalcogen-doped NGs and the sulfur-oxide were revealed by single-crystal X-ray diffraction analysis, and both P- and M-enantiomers of helicene enantiomers cocrystallize in a single crystal. Enantiomers of sulfur- and selenium-doped helical NGs were isolated by chiral HPLC. The chiroptical properties including ECD and CPL were investigated and the sulfur-embedded NG exhibited CPL activity with a g_{lum} of 1.1×10^{-3} at 480 nm and B_{CPL} of 13 M^{-1} cm^{-1}. The racemic barriers of S-NG and Se-NG were determined to be 29.6 and 31.2 kcal mol^{-1} respectively by HPLC-based thermal isomerization. The experimental and computational study including UV-vis absorption, fluorescence emission, efficiency, decay, HOMO–LUMO gaps, and charge distribution indicated that the chalcogen and its oxidative state in the NG significantly affect the electronic properties. The stability measurements of these NGs upon heating suggested that the Se-doped NG and its oxide undergo quantitative selenium-extrusion reactions, which offers dynamic control of the structural reconstruction. Notably, the highly distorted helical Se-oxide NG can transform to planar HBC under acidic conditions. The planar HBC generally exhibits low solubility and a high aggregation tendency in solvents. This HBS precursor would significantly facilitate the application of HBC in material fabrication.

Data availability

The full experimental details, synthetic procedures, characterization data, HPLC traces, UV-vis, fluorescence, IR and NMR spectra, computational details, and supplementary discussions associated with this article are provided in the ESI.†

Author contributions

Ranran Li performed most of the synthesis work and property studies. Bin Ma started the initial synthesis of compound $\mathbf{5_{O}}$. Shengtao Li helped with NMR, HPLC, and photophysical property measurements. P. An performed the DFT calculation and conceived the concept. P. An and C. Lu prepared and revised the manuscript. All the authors analyzed and interpreted the results.

Conflicts of interest

There are no conflicts to declare.

Acknowledgements

We are grateful for the financial support provided by the National Natural Science Foundation of China (21901226 and 22061046). We thank the advanced analysis and measurement center of Yunnan University for assistance with instrumentation. Particularly, we thank Dr Jie Zhou from the Advanced Analysis and Measurement Center of Yunnan University for the X-ray analysis.

Notes and references

1 (*a*) C. Wang, H. Dong, W. Hu, Y. Liu and D. Zhu, *Chem. Rev.*, 2012, **112**, 2208–2267; (*b*) K. S. Novoselov, V. I. Falko, L. Colombo, P. R. Gellert, M. G. Schwab and K. Kim, *Nature*, 2012, **490**, 192–200; (*c*) L. Zhang, Y. Cao, N. S. Colella, Y. Liang, J.-L. Brédas, K. N. Houk and A. L. Briseno, *Acc. Chem. Res.*, 2015, **48**, 500–509; (*d*) X.-Y. Wang, X. Yao and K. Müllen, *Sci. China: Chem.*, 2019, **62**, 1099–1144.

2 (*a*) Q. Miao, *Adv. Mater.*, 2014, **26**, 5541–5549; (*b*) N. Bachar, L. Liberman, F. Muallem, X. Feng, K. Müllen and H. Haick, *ACS Appl. Mater. Interfaces*, 2013, **5**, 11641–11653; (*c*) V. B. R. Pedersen, S. K. Pedersen, Z. Jin, N. Kofod, B. W. Laursen, G. V. Baryshnikov, C. Nuckolls and M. Pittelkow, *Angew. Chem., Int. Ed.*, 2022, **61**, e202212293.

3 (*a*) H.-A. Lin, Y. Sato, Y. Segawa, T. Nishihara, N. Sugimoto, L. T. Scott, T. Higashiyama and K. Itami, *Angew. Chem., Int. Ed.*, 2018, **57**, 2874–2878; (*b*) Q.-Q. Li, Y. Hamamoto, G. Kwek, B. Xing, Y. Li and S. Ito, *Angew. Chem., Int. Ed.*, 2022, **61**, e202112638; (*c*) Y.-F. Wu, S.-W. Ying, L.-Y. Su, J.-J. Du, L. Zhang, B.-W. Chen, H.-R. Tian, H. Xu, M.-L. Zhang, X. Yan, Q. Zhang, S.-Y. Xie and L.-S. Zheng, *J. Am. Chem. Soc.*, 2022, **144**, 10736–10742.

4 (*a*) T. Kawase and H. Kurata, *Chem. Rev.*, 2006, **106**, 5250–5273; (*b*) J. Wu, W. Pisula and K. Müllen, *Chem. Rev.*, 2007, **107**, 718–747; (*c*) W. Pisula, X. Feng and K. Müllen, *Chem. Mater.*, 2011, **23**, 554–567; (*d*) D. Bialas, E. Kirchner, M. I. S. Röhr and F. Würthner, *J. Am. Chem. Soc.*, 2021, **143**, 4500–4518; (*e*) N. Zhang, L. Yang, W. Li, J. Zhu, K. Chi, D. Chang, Y. Qiao, T. Wang, Y. Zhao, X. Lu and Y. Liu, *J. Am. Chem. Soc.*, 2022, **144**, 21521–21529; (*f*) L. Chai, Y.-Y. Ju, J.-F. Xing, X.-H. Ma, X.-J. Zhao and Y.-Z. Tan, *Angew. Chem., Int. Ed.*, 2022, **61**, e202210268; (*g*) S. Zank, J. M. Fernández-García, A. J. Stasyuk, A. A. Voityuk, M. Krug, M. Solà, D. M. Guldi and N. Martín, *Angew. Chem., Int. Ed.*, 2022, **61**, e202112834.

5 (*a*) M. Rickhaus, M. Mayor and M. Juríček, *Chem. Soc. Rev.*, 2017, **46**, 1643–1660; (*b*) S. H. Pun and Q. Miao, *Acc. Chem. Res.*, 2018, **51**, 1630–1642; (*c*) Y. Segawa, H. Ito and K. Itami, *Nat. Rev. Mater.*, 2016, **1**, 15002; (*d*) M. A. Majewski and M. Stępień, *Angew. Chem., Int. Ed.*, 2019, **58**, 86–116; (*e*) I. R. Márquez, S. Castro-Fernández, A. Millán and A. G. Campaña, *Chem. Commun.*, 2018, **54**, 6705–6718; (*f*) S. R. Peurifoy, T. J. Sisto, F. Ng, M. L. Steigerwald, R. Chen and C. Nuckolls, *Chem. Rec.*, 2019, **19**, 1050–1061; (*g*) Y.-T. Wu and J. S. Siegel, *Chem. Rev.*, 2006, **106**, 4843–4867; (*h*) R. A. Pascal, *Chem. Rev.*, 2006, **106**, 4809–4819; (*i*) A. Bedi and O. Godron, *Acc. Chem. Res.*, 2019, **52**, 2482–2490; (*j*) M. C. Stuparu, *Acc. Chem. Res.*, 2021, **54**, 2858–2870; (*k*) J. Wang, X. Zhang, H. Jia, S. Wang and P. Du, *Acc. Chem. Res.*, 2021, **54**, 4178–4190; (*l*) M. Grzybowski, B. Sadowski, H. Butenschön and D. T. Gryko, *Angew. Chem., Int. Ed.*, 2020, **59**, 2998–3027.

6 (*a*) M. Krzeszewski, Ł. Dobrzycki, A. L. Sobolewski, M. K. Cyrański and D. T. Gryko, *Angew. Chem., Int. Ed.*, 2021, **60**, 14998–15005; (*b*) H. Yokoi, Y. Hiraoka, S. Hiroto, D. Sakamaki, S. Seki and H. Shinokubo, *Nat. Commun.*, 2015, **6**, 8215.

7 (*a*) J. Luo, X. Xu, R. Mao and Q. Miao, *J. Am. Chem. Soc.*, 2012, **134**, 13796–13803; (*b*) P. An, R. Li, B. Ma, R.-Y. He, Y.-K. Zhang, M.-J. Xiao and B. Zhang, *Angew. Chem., Int. Ed.*, 2021, **60**, 24478–24483; (*c*) T. Kirschbaum, F. Rominger and M. Mastalerz, *Angew. Chem., Int. Ed.*, 2020, **59**, 270–274; (*d*) T. Kirschbaum, F. Rominger and M. Mastalerz, *Chem.–Eur. J.*, 2020, **26**, 14560–14564; (*e*) I. R. Márquez, N. Fuentes, C. M. Cruz, V. Puente-Muñoz, L. Sotorrios, M. L. Marcos, D. Choquesillo-Lazarte, B. Biel, L. Crovetto, E. Gómez-Bengoa, M. T. González, R. Martin, J. M. Cuerva and A. G. Campaña, *Chem. Sci.*, 2017, **8**, 1068–1074.

8 (*a*) N. Ogawa, Y. Yamaoka, H. Takikawa, K.-I. Yamada and K. Takasu, *J. Am. Chem. Soc.*, 2020, **142**, 13322–13327; (*b*) M. M. Martin, F. Hampel and N. Jux, *Chem.–Eur. J.*, 2020, **26**, 10210–10212; (*c*) J. Ma, Y. Fu, E. Dmitrieva, F. Liu, H. Komber, F. Hennersdorf, A. A. Popov, J. J. Weigand, J. Liu and X. Feng, *Angew. Chem., Int. Ed.*, 2020, **59**, 5637–5642; (*d*) X.-Y. Chen, J.-K. Li and X.-Y. Wang, *Chinese J. Org. Chem.*, 2021, **41**, 4105–4137.

9 (*a*) K. Y. Cheung, S. Gui, C. Deng, H. Liang, Z. Xia, Z. Liu, L. Chi and Q. Miao, *Chem*, 2019, **5**, 838–847; (*b*) S. Wang, J. Yuan, J. Xie, Z. Lu, L. Jiang, Y. Mu, Y. Huo, Y. Tsuchido and K. Zhu, *Angew. Chem., Int. Ed.*, 2021, **60**, 18443–18447.

10 M. Hermann, D. Wassy and B. Esser, *Angew. Chem., Int. Ed.*, 2021, **60**, 15743–15766.

11 (*a*) A. Jolly, D. Miao, M. Daigle and J.-F. Morin, *Angew. Chem., Int. Ed.*, 2020, **59**, 4624–4633; (*b*) J. M. Fernández-García, P. J. Evans, S. M. Rivero, I. Fernández, D. García-Fresnadillo, J. Perles, J. Casado and N. Martín, *J. Am. Chem. Soc.*, 2018, **140**, 17188–17196; (*c*) T. Fujikawa, D. V. Preda, Y. Segawa, K. Itami and L. T. Scott, *Org. Lett.*, 2016, **18**, 3992–3995; (*d*) R. Li, B. Ma, R.-Y. He, B. Zhang, Y.-K. Zhang, S.-Y. Feng and P. An, *Chem.–Asian J.*, 2022, **17**, e202101365.

12 (*a*) K. Kawasumi, Q. Zhang, Y. Segawa, L. T. Scott and K. Itami, *Nat. Chem.*, 2013, **5**, 739–744; (*b*) K. Kato, K. Takaba, S. Maki-Yonekura, N. Mitoma, Y. Nakanashi, T. Nashihara, T. Hata-Keyama, T. Kamada, Y. Hijikata, J. Pirillo, L. T. Scott, K. Yonekura, Y. Segawa and K. Itami, *J. Am. Chem. Soc.*, 2021, **143**, 5465–5469; (*c*) J. Wang, F. Gordillo Gámez, J. Marín-Beloqui, A. Diaz-Andres, X. Miao, D. Casanova, J. Casado and J. Liu, *Angew. Chem., Int. Ed.*, 2023, **62**, e202217124.

13 (*a*) M. Stępień, E. Gońka, M. Żyła and N. Sprutta, *Chem. Rev.*, 2017, **117**, 3479–3716; (*b*) M. Hirai, N. Tanaka, M. Sakai and S. Yamaguchi, *Chem. Rev.*, 2019, **119**, 8291–8331; (*c*) A. Borissov, Y. K. Maurya, L. Moshniaha, W.-S. Wong, M. Żyła-Karwowska and M. Stępień, *Chem. Rev.*, 2022, **122**, 565–788; (*d*) V. Barát and M. C. Stuparu, *Chem.–Asian J.*, 2021, **16**, 20–29; (*e*) V. Barát and M. C. Stuparu, *Chem.–Eur. J.*, 2020, **26**, 15135–15139; (*f*) X.-Y. Wang, X. Yao, A. Narita and K. Müllen, *Acc. Chem. Res.*, 2019, **52**, 2491–2505; (*g*) Y. Guo, C. Chen and X.-Y. Wang, *Chin. J. Chem.*, 2023, **41**, 1355–1373.

14 (*a*) J. Wu, W. Pisula and K. Müllen, *Chem. Rev.*, 2007, **107**, 718–747; (*b*) K. Müllen and J. P. Rabe, *Acc. Chem. Res.*, 2008, **41**, 511–520; (*c*) M. Grzybowski, K. Skonieczny, H. Butenschön and D. T. Gryko, *Angew. Chem., Int. Ed.*, 2013, **52**, 9900–9930; (*d*) H. Hölzel, P. Haines, R. Kaur, D. Lungerich, N. JUX and D. M. Guldi, *J. Am. Chem. Soc.*, 2022, **144**, 8977–8986.

15 (*a*) J. Wu, A. Fechtenkötter, J. Gauss, M. D. Watson, M. Kastler, C. Fechtenkötter, M. Wagner and K. Müllen, *J. Am. Chem. Soc.*, 2004, **126**, 11311–11321; (*b*) J. Wu, J. Li, U. Kolb and K. Müllen, *Chem. Commun.*, 2006, 48–50.

16 M. A. Medel, R. Tapia, V. Blanco, D. Miguel, S. P. Morcillo and A. G. Campaña, *Angew. Chem., Int. Ed.*, 2021, **60**, 6094–6100.

17 M. A. Medel, C. M. Cruz, D. Miguel, V. Blanco, S. P. Morcillo and A. G. Campaña, *Angew. Chem., Int. Ed.*, 2021, **60**, 22051–22056.

18 (*a*) B. Ma, M. Xiao, P. Liu and P. An, *Synlett*, 2022, **33**, 409–414; (*b*) B. Zhang, L. Ruan, Y.-K. Zhang, H. Zhang, R. Li and P. An, *Org. Lett.*, 2023, **25**, 732–737.

19 F. S. Guziec Jr and L. J. Sanfilippo, *Tetrahedron*, 1988, **44**, 6241–6285.

20 Deposition numbers 2238626–2238632 for compounds $\mathbf{5_{O}}$, **21**, **23**, $\mathbf{24_{SO}}$, $\mathbf{17_{S}}$, $\mathbf{18_{Se}}$, and $\mathbf{30_{HBC}}$ contain the supplementary crystallographic data for this paper.†

21 P. v. R. Schleyer, C. Maerker, A. Dransfeld, H. Jiao and N. J. R. van Eikema Hommes, *J. Am. Chem. Soc.*, 1996, **118**, 6317–6318.

22 (*a*) T. Lu and F. Chen, *J. Comput. Chem.*, 2012, **33**, 580–592; (*b*) W. Humphrey, A. Dalke and K. Schulten, *J. Mol. Graphics*, 1996, **14**, 33–38.

23 (*a*) Y. Shen and C.-F. Chen, *Chem. Rev.*, 2012, **112**, 1463–1535; (*b*) C. Li, Y. Yang and Q. Miao, *Chem.–Asian J.*, 2018, **13**, 884–894; (*c*) J. M. Fernández-García, P. J. Evans, S. Filippone, M. Á. Herranz and N. Martín, *Acc. Chem. Res.*, 2019, **52**, 1565–1574; (*d*) T. Mori, *Chem. Rev.*, 2021, **121**, 2373–2412; (*e*) Y. Wu, L. Zhang, Q. Zhang, S.-Y. Xie and L.-S. Zheng, *Org. Chem. Front.*, 2022, **9**, 4726–4743; (*f*) P. Karak and J. Choudhury, *Chem. Sci.*, 2022, **13**, 11163–11173; (*g*) G. R. Kiel, H. M. Bergman, A. E. Samkian, N. J. Schuster, R. C. Handford, A. J. Rothenberger, R. Gómez-Bombarelli, C. Nuckolls and T. D. Tillet, *J. Am. Chem. Soc.*, 2022, **144**, 23421–23427; (*h*) Y.-F. Wu, S.-W. Ying, S.-D. Liao, L. Zhang, J.-J. Du, B.-W. Chen, H.-R. Tian, F.-F. Xie, H. Xu, S.-L. Deng, Q. Zhang, S.-Y. Xie and L. S. Zheng, *Angew. Chem., Int. Ed.*, 2022, **61**, e202204334; (*i*) J.-K. Li, X.-Y. Chen, W.-L. Zhao, Y.-L. Guo, Y. Zhang, X.-C. Wang, A. C.-H. Sue, X.-Y. Cao, M. Li, C.-F. Chen and X.-Y. Wang, *Angew. Chem., Int. Ed.*, 2023, **62**, e202215367.

24 J. M. Fernández-Garcıía, P. Izquierdo-García, M. Buendía, S. Filip-pone and N. Martín, *Chem. Commun.*, 2022, **58**, 2634–2645.

25 (*a*) V. Boekelheide, I. D. Reingold and M. Tuttle, *J. Chem. Soc., Chem. Commun.*, 1973, 406–407; (*b*) R. S. Givens, R. J. Olsen and P. L. Wylie, *J. Org. Chem.*, 1979, **44**, 1608–1613; (*c*) A. Wakamiya, T. Nishinaga and K. Komatsu, *J. Am. Chem. Soc.*, 2002, **124**, 15038–15050; (*d*) T. Okamoto, K. Kudoh, A. Wakamiya and S. Yamaguchi, *Org. Lett.*, 2005, **7**, 5301–5304; (*e*) H. Kamiya, T. Kondo, T. Sakida, S. Yamaguchi and H. Shinokubo, *Chem.–Eur. J.*, 2012, **18**, 16129–16135; (*f*) P. R. Christensen, B. O. Patrick, E. Caron and M. O. Wolf, *Angew. Chem., Int. Ed.*, 2013, **52**, 12946–12950; (*g*) S. Hayakawa, K. Matsuo, H. Yamada, N. Fukui and H. Shinokubo, *J. Am. Chem. Soc.*, 2020, **142**, 11663–11668.